nature communications

Article

https://doi.org/10.1038/s41467-025-67281-8

Design of high-performance sustainable aluminum alloy series for laser additive manufacturing

Received: 22 February 2025

Accepted: 26 November 2025

Published online: 15 December 2025

Check for updates

Naoki Takata[1] ✉, Koki Minamihama[2], Takanobu Miyawaki[2], Yue Cheng[2], Yifan Xu[2], Wenyuan Wang[2], Dasom Kim[1], Asuka Suzuki[2], Makoto Kobashi[2] & Masaki Kato[3]

Lightweight Al alloys with enhanced mechanical properties are essential for structural applications across various industries. To promote sustainable material flow, this study introduces an Al-Fe-based multi-elemental alloy series optimized for laser-based additive manufacturing (AM) using powder bed fusion (PBF-LB), leveraging recycling-friendly Al alloys with Fe as a major impurity. The alloy design is based on the concept of elemental partitioning into either the liquid phase (forming metastable Al_6Fe phase for strengthening) or the solid phase (α-Al matrix) during solidification. Investigations of PBF-LB processed Al-Fe-X ternary alloys (X: Cu, Mn, and Ti) reveal the distinct roles of these alloying elements: Cu and Mn stabilize the Al_6Fe phase, while Ti enhances solid-solution strengthening, in the microstructure and associated mechanical properties. Additionally, Ti promotes grain refinement by inducing the heterogeneous nucleation of nanosized Al_3Ti-phase particles, leading to improved material ductility. The combined addition of alloy elements further stabilizes and strengthens the Al_6Fe phase (Cu and Mn). Moreover, Mn and Ti partition independently, enabling precise control of the α-Al/Al_6Fe two-phase microstructure, enhancing high-temperature mechanical performance. This study provides new insights for controlling refined metastable phases formed via PBF-LB, facilitating the development of high-performance, sustainable Al alloys for AM technologies.

Lightweight Al alloys are extensively used as structural materials in the aviation and transportation industries. Powder bed fusion with a laser beam (PBF-LB)[1–3], a metal additive manufacturing (AM) process, has recently gained prominence for fabricating complex geometrical metal components across various industrial applications[4–6]. The current industrial standards for Al alloys suitable for the PBF-LB process primarily comprise near-eutectic Al-Si alloys containing trace alloying elements[7–10]. Localized melting and subsequent rapid solidification (exceeding 10^4 K/s)[11,12] during the PBF-LB process lead to the formation of refined solidification microstructures. These microstructural features, including refined reinforcements and supersaturated solid solutions, not only enhance the performance of structural materials—such as high strength[13], fatigue resistance[14], wear resistance[15], and corrosion resistance[16,17]—but also result in anomalous mechanical behavior[18]. High-strength wrought-type Al alloys, such as the Al-Cu[19], Al-Mg-Si[20], and Al-Mg-Zn[21,22] alloy series, are highly susceptible to hot cracking[23,24] during solidification, leading to poor processability[25,26]. Nevertheless, the addition of an

[1]Department of Materials Design Innovation Engineering, Graduate School of Engineering, Nagoya University, Nagoya, Japan. [2]Department of Materials Process Engineering, Graduate School of Engineering, Nagoya University, Nagoya, Japan. [3]Aichi Center for Industry and Science Technology, Toyota-shi, Aichi, Japan. ✉e-mail: takata.naoki@material.nagoya-u.ac.jp

agent to enhance heterogeneous nucleation can prevent hot cracking in the PBF-LB process[21,22].

Al-Fe alloys are promising candidates for developing sustainable Al alloys[27,28] suitable for AM technologies. From the perspective of Al alloy recycling, composition requirements are shifting toward lower-purity-sensitive alloy powders produced from contaminated or mixed low-cost Al scraps, which contain certain impurity elements such as Fe, Mn, Cu, and Ti. Regarding Al scrap utilization, a recycling-friendly alloy design is essential to ensure a sustainable material flow compatible with AM technologies. Transition metals (TMs), which are major impurity elements in commercial Al alloys, are typically avoided because previous studies on cast alloys have demonstrated that the addition of transition metals often leads to the formation of coarse and brittle intermetallic phases[29], which adversely affect the mechanical performance of materials. However, Al-Fe binary alloys have been found to exhibit excellent PBF-LB processability and superior mechanical properties[30–32] due to the formation of a refined Al_6Fe metastable phase[33], which replaces the coarsened $Al_{13}Fe_4$ stable phase that is known for its brittleness. The rapid solidification inherent in the PBF-LB process enables this phase switching. Recent studies have shown that incorporating various transition metals (TMs) into AM Al-Fe alloys can enhance mechanical strength, particularly at high temperatures[34–43], while post-heat treatments can further improve thermal conductivity[44,45]. Consequently, Al-Fe-based multi-elemental alloy systems hold significant potential for developing sustainable, high-performance Al alloys tailored for AM technologies.

A promising strategy to further enhance the mechanical strength of solidified Al-Fe alloys is to promote the formation of the Al_6Fe metastable phase by adding alloying elements[46]. The incorporation of Mn or Cu facilitates partitioning into a refined Al_6Fe phase[33] (Fig. 1a, b) rather than an α-Al matrix, as Mn and Cu can form Al_6Mn[47] and $Al_{23}CuFe_4$ ($(Al, Cu)_6Fe$)[48] phases (Fig. 1c, d) in equilibrium with the α-Al phase[49,50]. This substitution occurs because Mn or Cu can replace Fe or Al sublattice sites within the Al_6Fe phase[51] (Fig. 1b). The thermodynamic stabilization induced by Cu or Mn addition increases the driving force for Al_6Fe-phase formation during solidification in the PBF-LB process, resulting in suppressed formation of the brittle $Al_{13}Fe_4$ phase. Another strategy for further strengthening involves introducing solute elements into the Al matrix during solidification. Supersaturated solute elements play a crucial role in solid-solution strengthening[13]. These insights present new opportunities for controlling solidification microstructures by manipulating elemental partitioning pathways in the PBF-LB process. This concept is schematically illustrated in the Al-X binary phase diagram (Fig. 1e). Element X with positive liquidus transient (m_X^L) values exhibits high partition coefficients ($k_X^{S/L} > 1$), leading to higher X concentrations in the solid α-Al phase during solidification (Fig. 1f). Conversely, element X with negative m_X^L values preferentially partitions into the liquid phase (Fig. 1f), resulting in enrichment within the liquid phase (resulting in the secondary solidified phase, such as the metastable Al_6Fe phase in Al-Fe alloy systems). This trend of elemental partitioning remains consistent even at the solid-liquid interface in non-equilibrium conditions, where the solidification rate in the PBF-LB process typically ranges from 0.01 to 1 m/s[34,52]. This behavior is described by the velocity-dependent partition coefficient (k_v) based on the Aziz model[34,53] (Fig. 1g). In most cases, element X with a positive or negative m_X^L value (corresponding to $k_X^{S/L} > 1$ or $k_X^{S/L} < 1$) can be categorized based on the solidification reaction type, specifically peritectic or eutectic reaction in Al-X binary systems. Consequently, the role of alloying elements in the formation of the α-Al/Al_6Fe two-phase microstructures (Fig. 1a) can be systematically organized using the periodic table, as illustrated in Fig. 1h. Although numerous elements fall into the eutectic reaction category (partitioning into the liquid phase), TMs of groups 4, 5, and 6 predominantly undergo peritectic reactions, leading to their partitioning into the α-Al matrix and contributing to solid-solution strengthening. Notably, the α-Al phase exhibits a high solubility limit for Ti, combined with low diffusivity[54], indicating strong potential for strengthening AM Al-Fe-based alloys, even in high-temperature environments[34,42].

The discussed strategies, based on thermodynamics and kinetics, can provide a novel concept for alloy design in AM technologies. Following the concept (Fig. 1h), several TM elements were selected for Al-Fe-based multi-elemental systems: Cu and Mn (eutectic type, stabilizing the Al_6Fe phase) and Ti (peritectic type, with high solubility). This study systematically examines the role of alloying elements in shaping the microstructure and mechanical properties of Al-Fe-X ternary alloys. Accordingly, an efficient strategy for developing a novel high-performance Al-Fe alloy series optimized for AM technologies is proposed.

Results

Role of alloying elements: Al-Fe-X ternary alloys

The multiscale microstructures of the Al-Fe binary alloy and Al-Fe-X (X: Cu, Mn, Ti) ternary alloys processed by PBF-LB under optimized laser conditions (Supplementary Fig. 1 and Table 1) are presented in Fig. 2. The compositions of the ternary alloy were designed based on thermodynamic calculations, as discussed in Supplementary Information (Supplementary Fig. 2). Representative inverse-parabolic melt-pool cross-sections were observed in all experimental alloys manufactured through PBF-LB (Fig. 2a). Scanning electron microscopy (SEM) backscattered electron images revealed columnar grains several micrometers in width within the melt pools of the Al-Fe binary alloy. Similar grain morphologies were observed in the Al-Fe-Cu[45] and Al-Fe-Mn[55] ternary alloys. Conversely, the Al-Fe-Ti ternary alloy exhibited finer grains with an equiaxed morphology (Fig. 2b). This feature was evidently revealed by electron backscattered diffraction (EBSD) analysis of the α-Al matrix (Fig. 2c). The Al-Fe, Al-Fe-Cu, and Al-Fe-Mn alloys exhibited numerous elongated grains with a <011> orientation along the building direction (BD). However, the Al-Fe-Ti alloy exhibited a refined grain morphology with a relatively randomized crystallographic texture. The equivalent grain size (d_{eq}) of the Al-Fe-Ti alloy was significantly smaller than that of the other alloys. The grain refinement of the Al-Fe-Ti alloy during the PBF-LB process was attributed to the heterogeneous nucleation on the nanosized particles of a primary Ti-rich intermetallic phase (Supplementary Fig. 3), presumably the Al_3Ti phase, which exhibited a slight lattice mismatch with the α-Al phase[56]. This observation aligned well with previous reports on facilitated grain refinement in Al alloys containing Sc and Zr, due to the formation of primary solidified Al_3X ($L1_2$) phases[57]. The morphologies of Al_6Fe-phase particles within the melt pools (Fig. 2d) and near the melt-pool boundaries (Fig. 2e) were analyzed using transmission electron microscopy (TEM). Numerous spherical (and locally extended) Al-Fe intermetallic phases, with sizes ranging from a few tens of nanometers, were observed throughout the melt-pool structure. The morphology slightly changed with adding Cu and Mn (Fig. 2d). In the Al-Fe-Cu alloy[45], numerous nanoscale precipitates were observed in the interspace between granular intermetallic phases. Notably, quantitative image analyses revealed that the mean size of nanoscale precipitates was approximately 10 nm. In the Al-Fe-Mn alloy[55], these intermetallic phases are often connected to form a network-like structure, indicating an increased fraction of intermetallic phase with Mn addition. The addition of Ti had minimal influence on the morphology. In all experimental alloys, relatively coarsened cellular structures with a spacing of approximately a few hundred nanometers were locally formed at the melt-pool boundaries (Fig. 2e). The Al-Fe intermetallic phases were identified as the Al_6Fe phase (*oC*28) through X-ray diffraction (XRD) (Supplementary Fig. 4 and previous studies[54]) and electron diffraction analyses[45,55].

A detailed chemical composition analysis of each alloy sample was conducted using scanning transmission electron microscopy (STEM) equipped with energy-dispersive X-ray spectroscopy (EDS). The results

https://doi.org/10.1038/s41467-025-67281-8

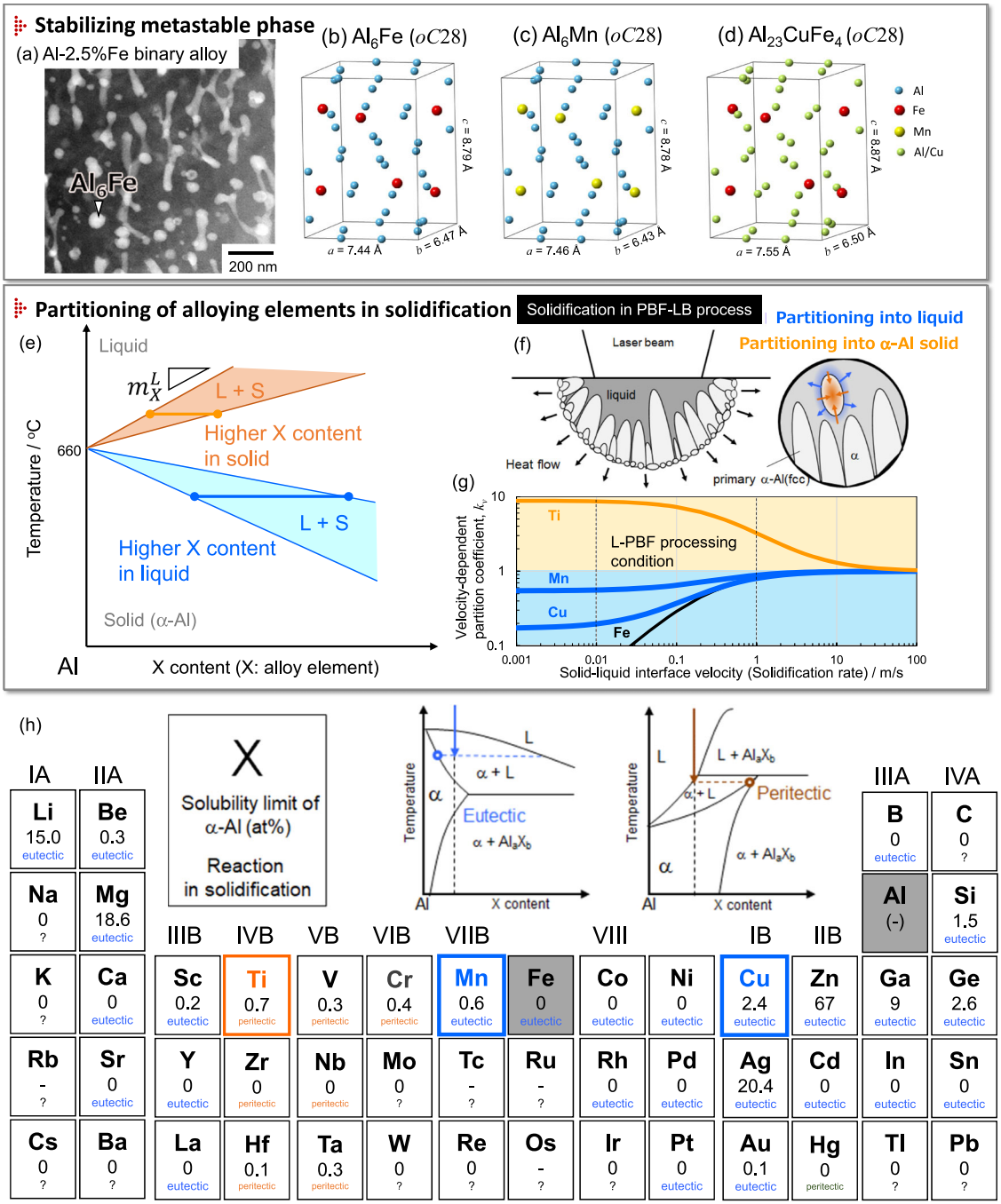

Fig. 1 | Design concept of Al-Fe multi-elemental systems suitable for the PBF-LB process. a α-Al/Al_6Fe two-phase nanostructure of Al-2.5% Fe binary alloy[33]. **b**–**d** Crystal structures of Al_6Fe, Al_6Mn, and $Al_{23}CuFe_4$ phases (tetragonal *oC*28)[46]. **e** Varied partitioning of alloying elements depending on liquidus transients (m_X^L) in Al alloys. **f** Schematic of elemental partitioning during solidification. **g** Varied partition coefficients of various elements depending on solidification rate (velocity-dependent partition coefficient, k_v), calculated based on the Aziz model[53] (The source data are provided as a Source Data file). **h** Reaction type in solidification and solubility limits of elements in the Al-X binary system, labeled on the periodic table.

are presented in Fig. 3. The representative microstructures at the melt-pool boundaries indicated that the added Cu and Mn were enriched in the Al_6Fe intermetallic phases (Fig. 1b) of the Al-Fe-Cu and Al-Fe-Mn alloys (Fig. 3a, b). A quantitative composition analysis of the Al_6Fe phases revealed the formation of $(Al, Cu)_6Fe$ and $Al_6(Fe, Mn)$ phases (Fig. 3d, e) in the Al-Fe-Cu and Al-Fe-Mn alloys, respectively. This finding suggested that Cu and Mn partitioned preferentially into the Al_6Fe phase during solidification. The replacement of Fe sublattice sites with Mn suggested an increase in the Al_6Fe-phase fraction, which corresponded to the observed morphology of the Al_6Fe phase in the Al-Fe-Mn alloy (Fig. 2d). Notably, the quantified composition of the $(Al, Cu)_6Fe$ phase (Fig. 3d) corresponded well with the composition of the $Al_{23}CuFe_4$ phase (Fig. 1d), which was in equilibrium with the α-Al matrix in the Al-Fe-Cu ternary system[49]. Such results are consistent with the experimentally measured fractions of the Al_6Fe phase when Cu or Mn elements are added (Supplementary Table 2). Conversely, Ti partitioned into an α-Al matrix rather than Al_6Fe-phase particles (Fig. 3c), resulting in a negligible amount of Ti in the Al_6Fe phase of the Al-Fe-Ti alloy (Fig. 3f). These experimental results demonstrated that the partitioning behavior of the added alloying elements followed the reaction trends observed in Al-X binary systems (Fig. 1h), even under rapid solidification conditions at high solid-liquid interface velocities

https://doi.org/10.1038/s41467-025-67281-8

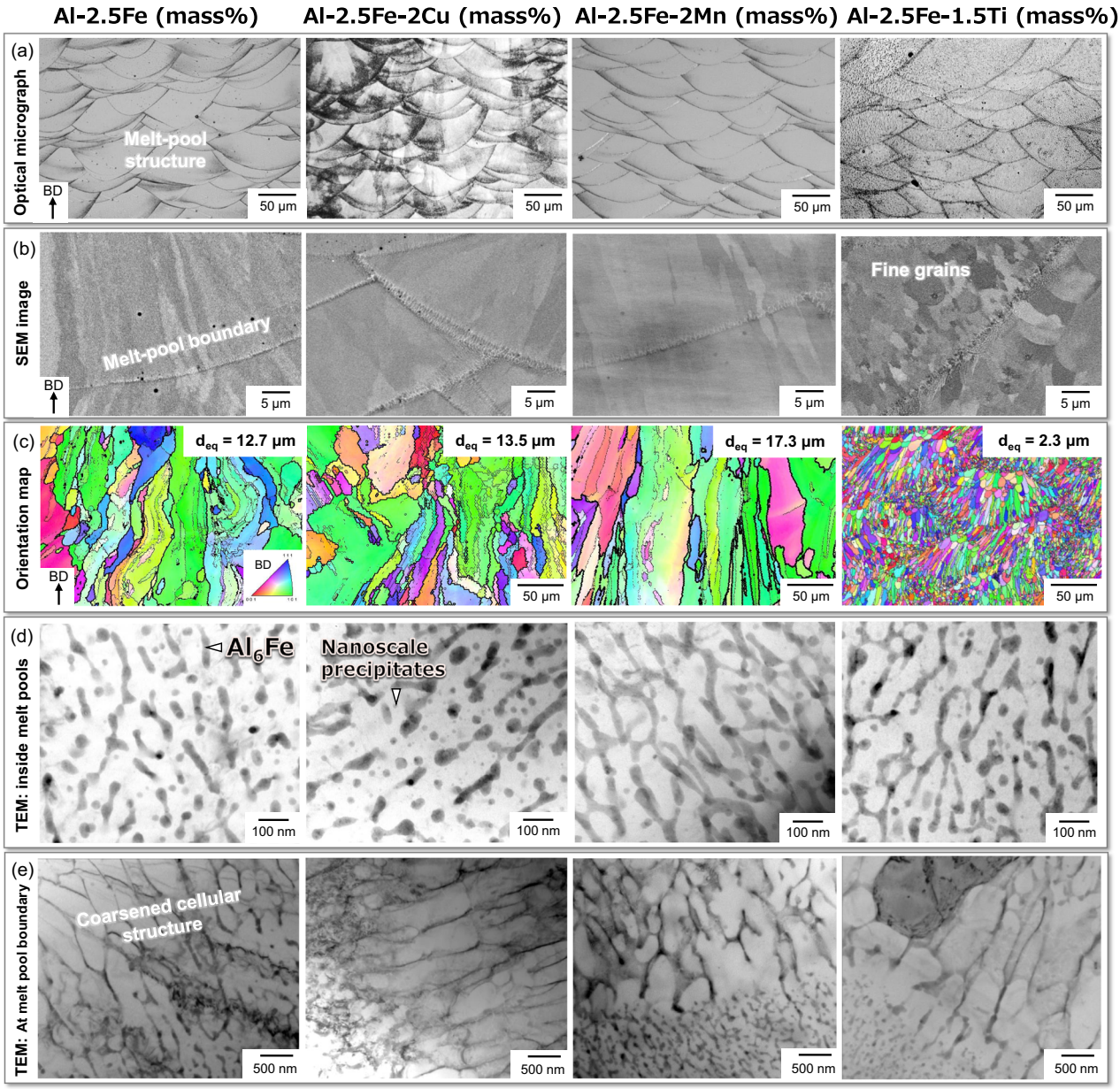

Fig. 2 | Multiscale microstructures of Al-Fe binary and Al-Fe-X ternary alloys (X: Cu, Mn, and Ti) additive manufactured via PBF-LB. a Optical micrographs showing melt-pool structures. **b** SEM images showing grain morphologies. **c** EBSD orientation distribution map for α-Al matrix (crystallographic orientation parallel to building direction (BD) is colored according to the attached unit triangle of inverse pole figure). TEM bright-field images showing the morphologies of the Al_6Fe-phase particles **d** inside melt pools or **e** near melt-pool boundaries.

ranging from 0.01 to 1 m/s[34,52](Fig. 1g) during the PBF-LB process. Quantitative composition measurements at different locations within the melt-pool structures (Fig. 3g) revealed that the solute Fe content was higher inside the melt pool (approximately 1.1%) than in the relatively coarsened cellular structures localized at melt-pool boundaries (approximately 0.4%), with minimal dependence on the addition of a third element. The measured solute Fe content exceeded the equilibrium solubility limit (approximately 0.1%). Notably, the lower solute Fe content at the melt-pool boundaries supported a low velocity-dependent partition coefficient (k_v)[53] for Fe (Fig. 1g), attributable to the low solidification rates at the onset of solidification[11,34,52] (Fig. 1f). Local variations in solute Cu and Mn contents were observed in Al-Fe-X ternary alloys. However, the opposite trend was observed for solute Ti (Fig. 3h), indicating enhanced Ti partitioning into the solidified α-Al phase at lower solidification rates. The measured compositions of the α-Al and Al_6Fe phases can assess experimental partition coefficients ($k_X^{S/L}$) at high solidification rates in the PBF-LB process. The assessed $k_{Cu}^{S/L}$, $k_{Mn}^{S/L}$, and $k_{Ti}^{S/L}$ values were 0.24, 0.44, and 5.0, respectively. These results were consistent with the k_v values in the solidification rate range of the PBF-LB process (Fig. 1g) based on the Aziz model[34,53]. The obtained results confirmed the validity of the proposed concept of alloy design for controlling the distribution of alloying elements in refined microstructures using the PBF-LB process.

To investigate the effect of third-element additions on the mechanical properties of Al-Fe-X alloys, tensile tests were performed at temperatures ranging from 20 to 300 °C (Fig. 4). At ambient temperature (Fig. 4a, b), the Al-Fe binary alloy specimens exhibited variations in yield strength and tensile ductility depending on whether the tensile direction (TD) was perpendicular or parallel to the building direction (BD). Particularly, the observed anisotropic tensile ductility was attributed to localized deformation and fracture along the soft melt-pool boundaries[58], which contained coarse microstructures

https://doi.org/10.1038/s41467-025-67281-8

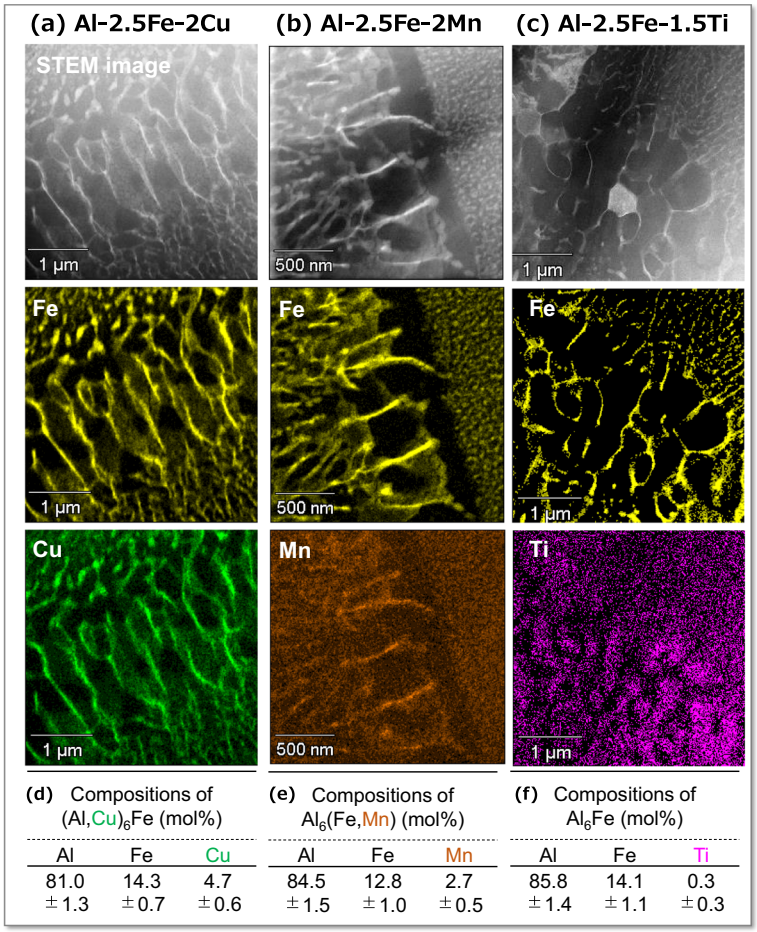

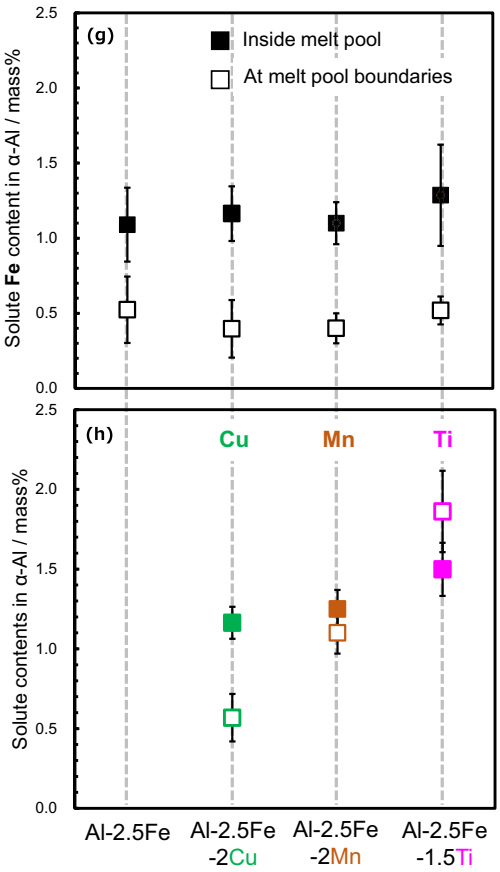

Fig. 3 | Partitioning of alloying elements in refined α-Al/Al_6Fe two-phase microstructures formed via PBF-LB. a–c Representative STEM-EDS element distribution maps of Al-Fe-Cu, Al-Fe-Mn, and Al-Fe-Ti ternary alloys. **d–f** Quantified composition of the Al_6Fe phase. **g** Solute Fe contents and **h** solute contents of third elements at different locations of the melt-pool structure.

(Fig. 2e). Similar anisotropic mechanical properties were observed in the Al-Fe-Mn and Al-Fe-Cu ternary alloys. The addition of Mn and Cu enhanced both the yield and tensile strengths (exceeding 350 MPa) by increasing strain hardening. The increase in yield strength upon Mn addition was attributed to the contribution of a higher fraction of Al_6(Fe, Mn) phase particles to strengthening. Conversely, the enhanced strain hardening observed in the Cu-containing alloy was attributed to the introduction of nanoscale precipitates with a mean size of approximately 10 nm in the interspace between the (Al, Cu)$_6$Fe phases (Fig. 1d). Notably, Al-Fe-Ti alloy exhibited both relatively higher strength (presumably due to the high solute Ti concentration; Fig. 3h) and significantly improved tensile elongation of approximately 15%, which was independent of the TD-BD relationship. This corresponded well to the fracture surfaces of the tensile-ruptured specimens (Supplementary Fig. 5). The isotropic tensile ductility in this alloy was attributed to grain refinement, which was facilitated by heterogeneous nucleation enhanced by Ti addition (Supplementary Fig. 3). Although the strength decreased with increasing temperature (Fig. 4c, d), the reduction was less pronounced compared to conventional Al alloys used in AM[8,34,42], as presented in Supplementary Fig. 6. Particularly, the Al-Fe-Mn alloy maintained a high yield strength (exceeding 220 MPa) at 300 °C (Fig. 4e). Conversely, the strength of the Al-Fe-Cu alloy decreased more significantly with increasing temperature. This accelerated weakening at elevated temperatures could be attributed to the coarsening of nanoscale precipitates containing Cu, which exhibited relatively high diffusivity compared to Fe, Mn, and Ti[51]. This phenomenon could also explain the temperature-dependent variations in tensile ductility observed in the Al-Fe-Cu alloy specimens (Fig. 4f). These findings indicate that tailoring the Al_6Fe phase through Mn and Cu additions significantly impacts the mechanical strength. Notably, Mn and Cu played distinct roles in the strengthening mechanisms, particularly in terms of high-temperature mechanical performance. While Cu contributed to strain hardening via nanoscale precipitates, Mn enhanced the Al_6 (Fe, Mn) phase fraction for solid-solution and precipitation strengthening. Conversely, Ti addition strengthened the alloy via solute Ti hardening while simultaneously improving tensile ductility through grain refinement. Supplementary Table 3 summarizes the mechanical properties and measurement deviations of the Al-Fe-X (Cu, Mn, and Ti) alloy specimens.

Discussion

Combined effect of alloying elements: further enhanced formation of Al_6Fe phase

This study demonstrated the partitioning of the added Cu and Mn within the refined Al_6Fe phase formed during solidification in the PBF-LB process (Fig. 3). The presence of Cu and Mn provided a significant driving force for Al_6Fe phase formation, enhancing the strengthening effect and resulting in superior tensile strength in the Al-Fe-Cu and Al-Fe-Mn ternary alloys (Fig. 4). These findings underscore the potential for designing high-strength Al-Fe-Cu-Mn quaternary alloys optimized for PBF-LB by incorporating both Cu and Mn to stabilize the Al_6Fe phase (Fig. 1h).

A gas atomization process was used to prepare alloy powder with the following composition: Al-2.5Fe-2Cu-2Mn (mass%). The PBF-LB

https://doi.org/10.1038/s41467-025-67281-8

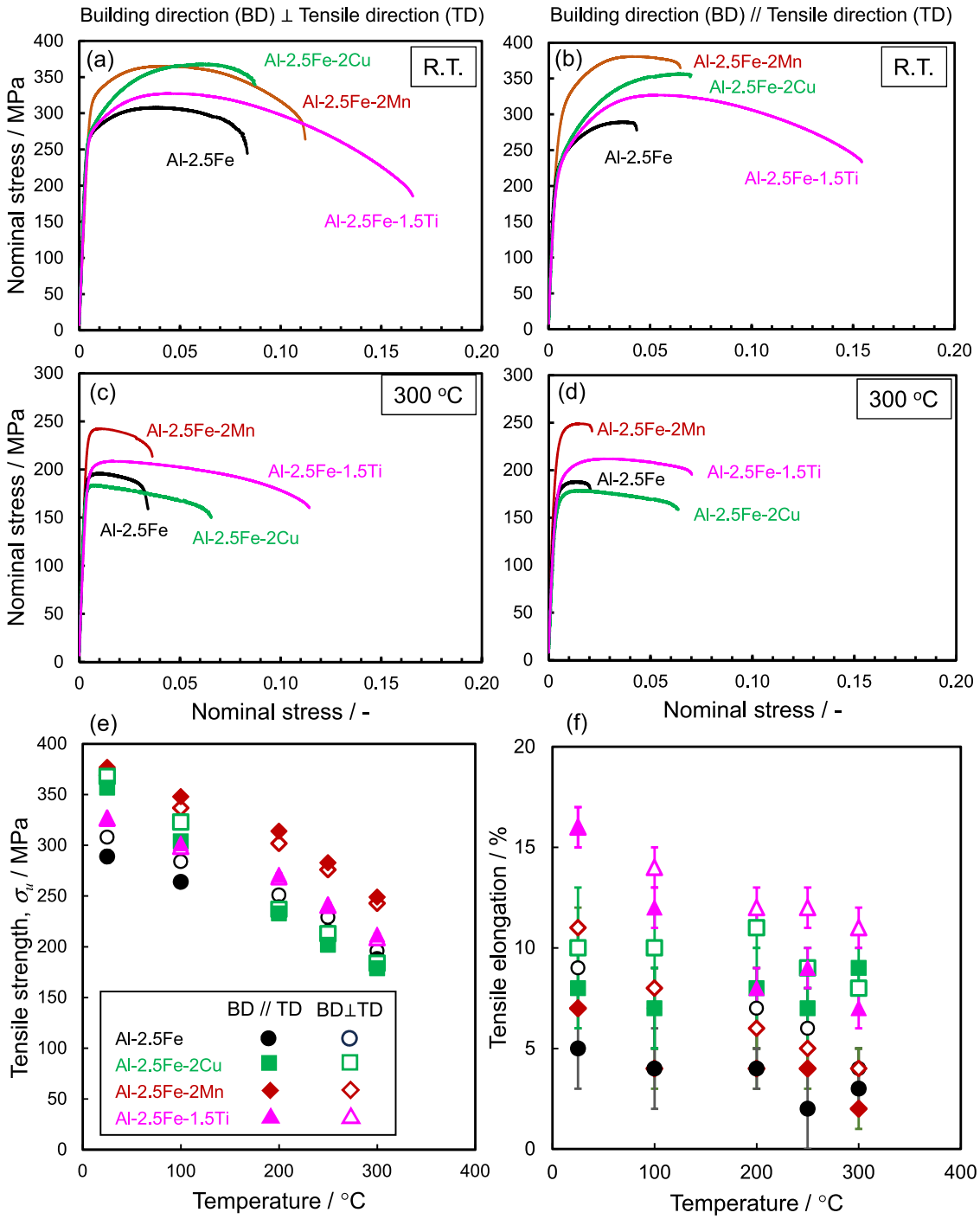

Fig. 4 | Mechanical properties of Al-Fe-X (X: Cu, Mn, and Ti) ternary alloys additive manufactured by PBF-LB. a–d Nominal stress–strain curves of the specimens tensile-deformed perpendicular or parallel to the building direction (TD // BD or TD⊥BD) at room temperature (approximately 20 °C) and 300 °C. **e**, **f** Changes in tensile strength and ductility as functions of test temperature (Error bars show the maximum and minimum values of the mechanical data measured three times). The source data are provided as a Source Data file.

processing parameters were then optimized to fabricate alloy samples with high relative densities exceeding 99% (Supplementary Fig. 7). The results of multiscale microstructural characterizations and tensile testing of the Al-Fe-Cu-Mn alloy processed under optimal conditions are shown in Fig. 5. A representative melt-pool structure (Fig. 5a) revealed elongated α-Al grains oriented along BD (Fig. 5b), consistent with observations in the Al-Fe-Cu and Al-Fe-Mn ternary alloys (Fig. 2a, c). Both Cu and Mn were enriched in the refined Al_6Fe phase, as confirmed by XRD (Supplementary Fig. 8), and their partitioning was evident inside the melt pool (Fig. 5d) and at the melt-pool boundaries (Fig. 5e). Notably, nanoscale precipitates were observed within the α-Al matrix as well as the Al-Fe-Cu ternary alloy (Fig. 2d). Quantitative composition analyses (Fig. 5c) revealed that Cu and Mn replaced Fe sublattice site in the Al_6Fe phase, forming the Al_6(Fe, Cu, Mn) phase. This substitution suggested that the interaction of Mn with Cu promoted the occupation of Fe sublattice sites in the Al_6Fe structure (Fig. 1b). Additionally, solute contents of alloy elements were higher inside the melt pool than at the melt-pool boundaries (Fig. 5c), aligning with the variations in k_v values of Fe, Cu, and Mn as a function of the solidification rate (Fig. 1g). The effect of combined Cu and Mn

https://doi.org/10.1038/s41467-025-67281-8

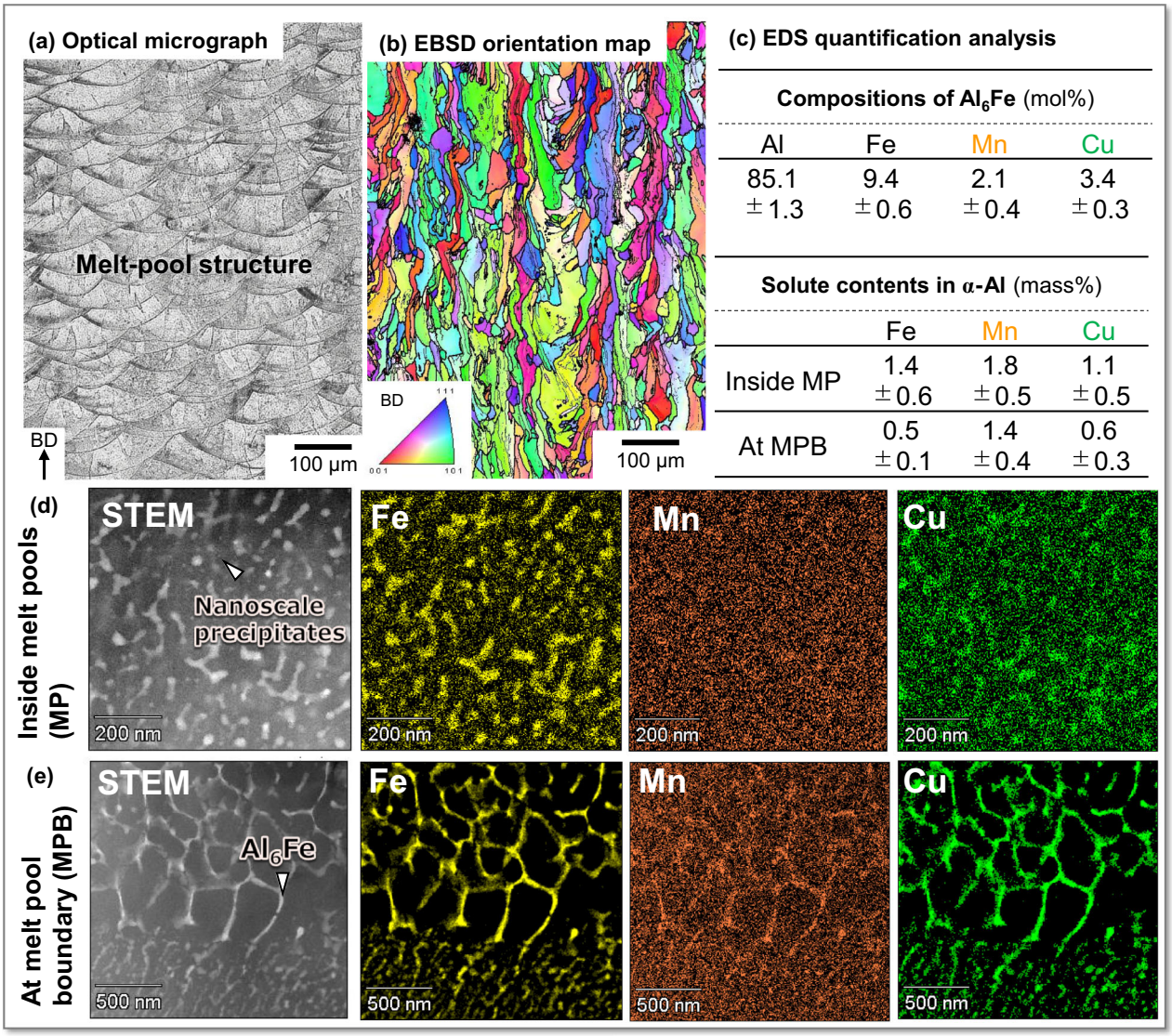

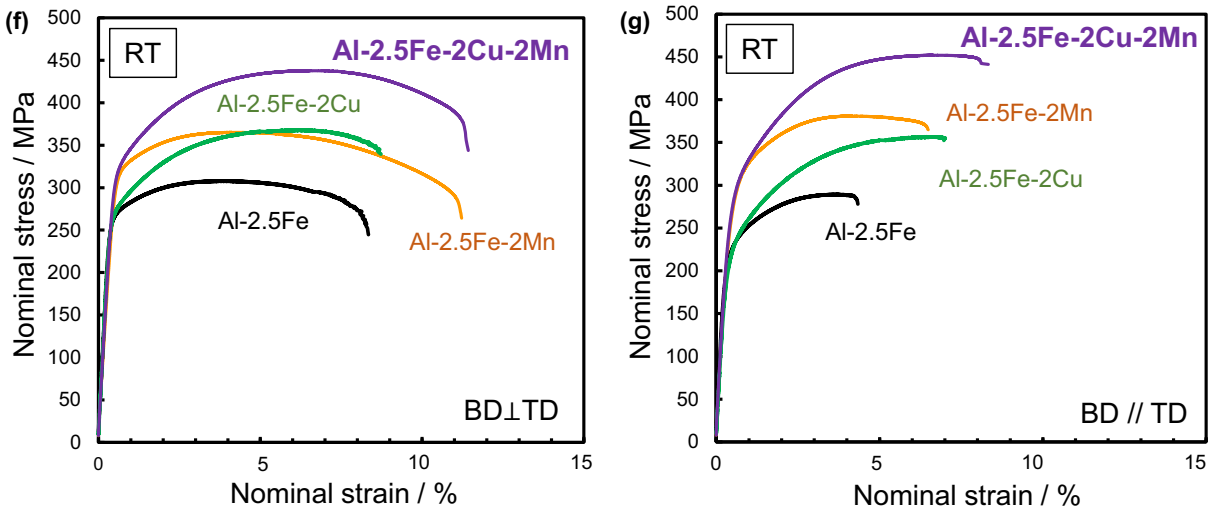

Fig. 5 | Multiscale microstructures and mechanical properties of Al-Fe-Cu-Mn quaternary alloys additive manufactured via PBF-LB. a Optical micrographs showing melt-pool structures. **b** EBSD orientation distribution map for the α-Al matrix (crystallographic orientation parallel to the BD is colored based on the attached unit triangle of inverse pole figure). **c** Quantified compositions of the Al_6Fe phase and solute contents of alloy elements. **d**, **e** Representative STEM-EDS element distribution maps. **f**, **g** Nominal stress–strain curves obtained from the tensile tests of specimens deformed perpendicular or parallel to the building direction (The source data are provided as a Source Data file).

https://doi.org/10.1038/s41467-025-67281-8

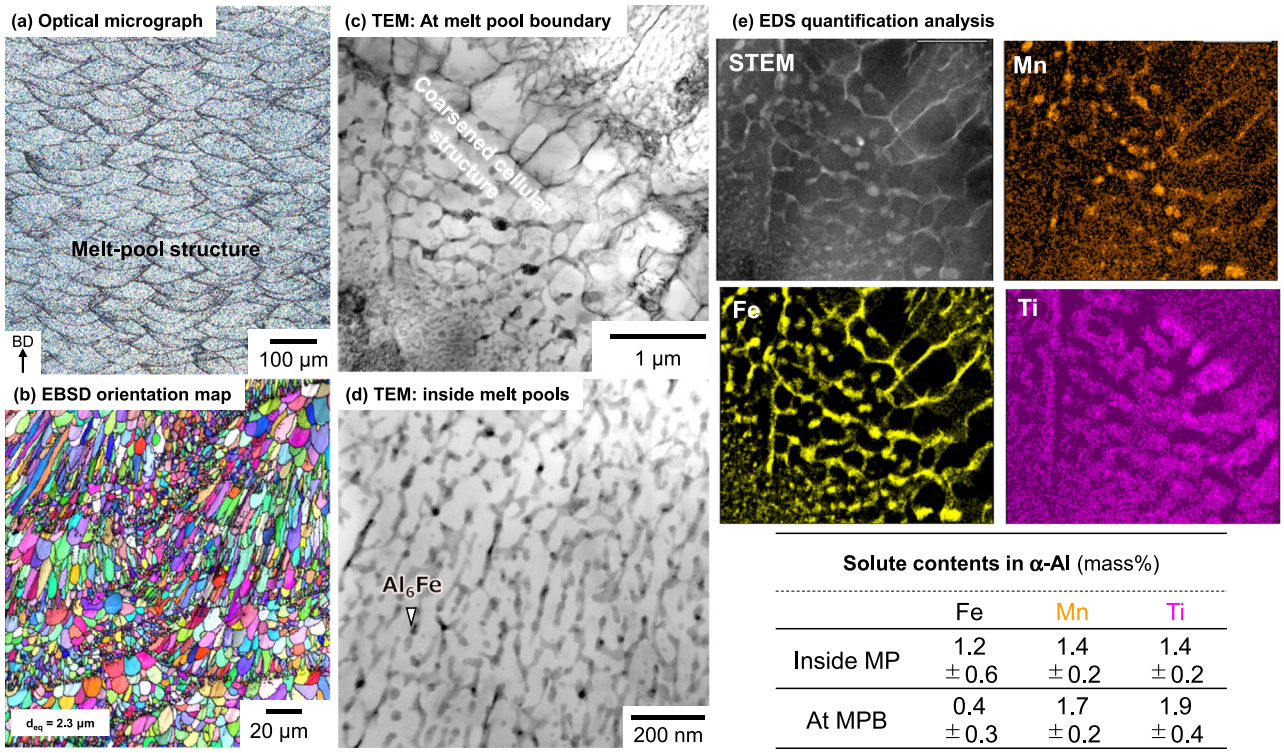

Solute contents in α-Al (mass%)

	Fe	Mn	Ti
Inside MP	1.2 ± 0.6	1.4 ± 0.2	1.4 ± 0.2
At MPB	0.4 ± 0.3	1.7 ± 0.2	1.9 ± 0.4

Fig. 6 | Multiscale microstructures of Al-Fe-Mn-Ti quaternary alloy additive manufactured via PBF-LB. a Optical micrographs showing melt-pool structures. **b** EBSD orientation distribution map for the a-Al matrix (crystallographic orientation parallel to the BD is colored). **c**, **d** TEM images of microstructure at the melt-pool boundary and inside the melt pools. **e** STEM-EDS element distribution maps and EDS measured contents of solute elements.

additions on room-temperature tensile properties was evident in the Al-Fe-Cu-Mn quaternary alloy specimens (Fig. 5f, g; Supplementary Table 3). Although anisotropic tensile ductility was observed, the Al-Fe-Cu-Mn alloy specimens exhibited increased yield strength due to the addition of Mn and enhanced strain hardening due to the addition of Cu, achieving a high tensile strength of approximately 450 MPa. The enhanced strain hardening resulted in adequate tensile ductility by increasing uniform elongation. According to the results of Al-Fe-X ternary alloys (Figs. 2 and 4), the simultaneous improvement in yield strength and strain hardening could be attributed to increased Al_6Fe-phase fraction (by Mn addition) and numerous nanoscale precipitates (by Cu addition) in Al-Fe-Cu-Mn ternary alloy specimens. These results demonstrate that incorporating alloying elements with similar roles (such as eutectic stabilizers of the Al_6Fe phase, as indicated in Fig. 1h) can serve as an effective strategy for designing Al-Fe-based multi-elemental alloys with superior mechanical performance tailored for PBF-LB processes.

Combined effect of alloying elements: towards high-temperature applications

The proposed concept (Fig. 1) introduces a novel approach to alloy design for high-temperature applications. One of the key factors in achieving superior mechanical performance in materials exposed to harsh environments for extended periods is the thermal stability of their microstructural morphology[59]. This study demonstrated that Cu, which exhibits higher diffusivity than Fe and Mn[54], significantly reduced high-temperature strength (Fig. 4e). Contrarily, Mn effectively stabilized the Al_6Fe phase at elevated temperatures, making it a critical element for maintaining microstructural integrity. Conversely, Ti exhibited a relatively high solubility limit (Fig. 1h) and underwent a peritectic reaction, leading to preferential partitioning into the α-Al phase during solidification (Fig. 3c). This behavior suggested that solute Ti, with its inherently low diffusivity[53], inhibited the growth and coarsening of the refined Al_6Fe phase at elevated temperatures. Additionally, previous studies have reported that solute Ti can stabilize fine precipitation morphologies, further contributing to thermal stability[59,60]. Assuming minimal interaction between Mn and Ti during solidification, Mn was expected to partition into the Al_6Fe phase, while Ti was preferentially incorporated into the α-Al phase. Consequently, the combined addition of Mn and Ti with low diffusivities thermally stabilized the refined α-Al/Al_6Fe two-phase microstructure and achieved superior high-temperature mechanical performance.

The proposed concept of controlled elemental partitioning was used to fabricate an Al-2.5Fe-2Mn-1.5Ti (mass%) quaternary alloy, which was then used for preparing material powder by a gas atomizing process. Preliminary experiments allowed for the optimization of the PBF-LB processing parameters for manufacturing the fully dense alloy samples with high relative densities above 99 % (Supplementary Fig. 7). The results of the multiscale microstructural characterizations of the Al-Fe-Mn-Ti alloy fabricated via PBF-LB process under optimal processing conditions are shown in Fig. 6. A refined grain morphology (d_{eq} = 2.3 μm) with a relatively randomized crystallographic texture (Fig. 6b) was observed inside the melt-pool structure (Fig. 6a). The microstructural feature was observed in the Al-Fe-Ti ternary alloy, which was indicative of heterogeneous nucleation upon the formation of nanosized Al_3Ti-phase particles during solidification (Supplementary Fig. 9). The morphologies of the Al_6Fe-phase particles (Fig. 6c, d, Supplementary Fig. 10) were identical to those of the Al-Fe-Mn and Al-Fe-Ti ternary alloys (Fig. 2e, d). An EDS composition analysis revealed the enrichment of Mn and Ti in the Al_6Fe and α-Al phases, respectively (Fig. 6e). The variation in the solute Mn and Ti contents based on the location of the melt-pool structure (Fig. 6e) corresponded well with the trend of the ternary alloys (Fig. 3g, h). These results demonstrated that the partitioning of alloy elements with distinct roles (eutectic or peritectic, as illustrated in Fig. 1) was independently controlled during solidification via PBF-LB. The mechanical properties of the PBF-LB-

https://doi.org/10.1038/s41467-025-67281-8

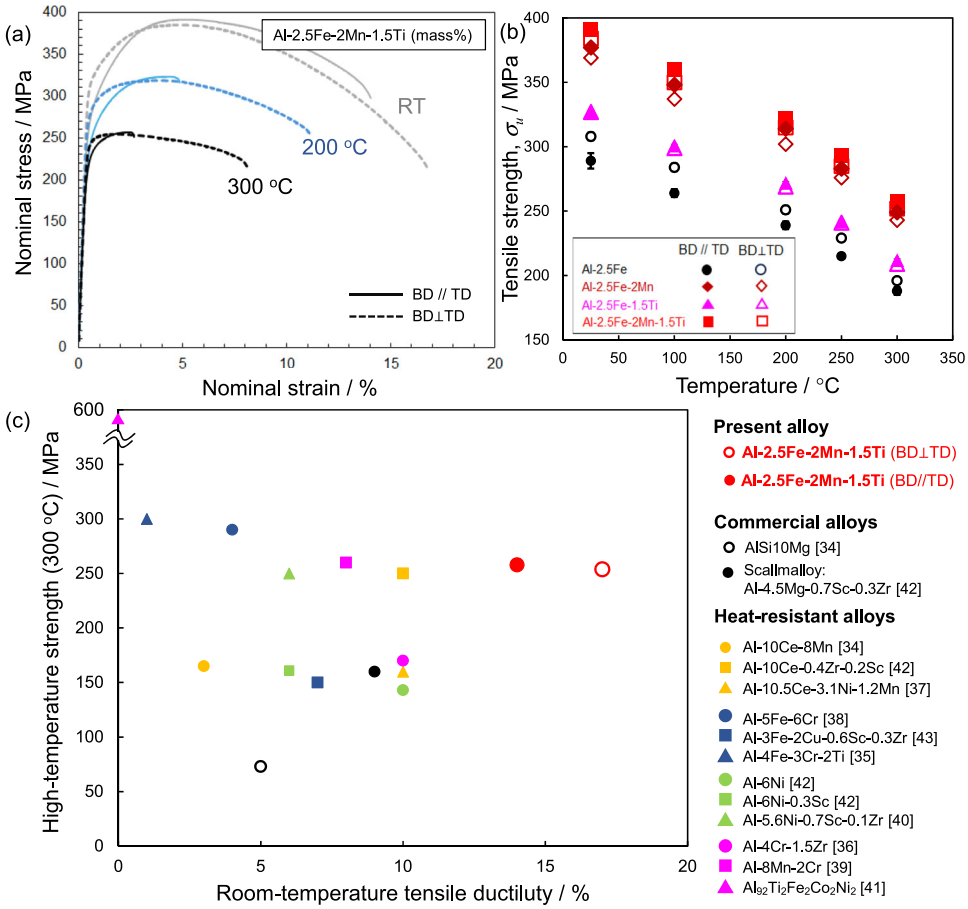

Fig. 7 | Mechanical performance of Al-Fe-Mn-Ti quaternary alloy additive manufactured via PBF-LB. a Nominal stress–strain curves obtained from the tensile tests at different temperatures. **b** Variations in tensile strength as a function of test temperature (Error bars show the maximum and minimum values of the mechanical data measured three times). **c** Balancing high-temperature strength and room-temperature ductility with developed Al alloys manufactured through the PBF-LB process[34–43]. The source data are provided as a Source Data file.

based Al-Fe-Mn-Ti alloy are summarized in Fig. 7. The Al-Fe-Mn-Ti alloy specimen exhibited a higher tensile strength of approximately 390 MPa (Fig. 7a) than the Al-Fe-Mn and Al-Fe-Ti ternary alloy specimens (Fig. 4a, b). Notably, the room-temperature ductility (14–17% total elongation) was dependent on the relationship between the TD and BD (Fig. 7a), presumably due to the grain refinement by Ti addition (Fig. 6a). Although the anisotropy in tensile ductility appeared more significant at higher test temperatures (Fig. 7a) due to the preferential fracture along melt-pool boundaries (Supplementary Fig. 11), high strength (exceeding 250 MPa) was maintained at 300 °C, which was superior to those of the ternary alloy specimens (Fig. 7b). The Al-Fe-Mn-Ti alloy exhibited a superior balance of high-temperature strength and room-temperature ductility (Fig. 7c) compared to various heat-resistant Al alloys developed under the LB-PBF process[34–43]. A comparative study confirmed the high reliability of the newly designed Al-Fe-Mn-Ti alloy as a mechanically robust material for use at ambient (in post-processing) and high temperatures (in service). In addition, the hardness and high-temperature mechanical properties almost remained unchanged even after a long-term thermal exposure (at 300 °C for 100 h). Such a stable mechanical strength could originate from the high thermal stability of the refined $Al_6(Fe, Mn)$ phase in the α-Al matrix containing solute Ti with low diffusivity (Supplementary Fig. 12).

In summary, this study presents a novel design concept for Al-Fe-based multi-elemental alloys—a recycling-friendly Al alloy series that supports sustainable material flow—suitable for the PBF-LB process. The design is based on the selective partitioning of elements into the liquid phase (promoting the formation of the Al_6Fe metastable phase for strengthening) or the solid phase (stabilizing the α-Al matrix) during solidification. It was demonstrated that the Al-Fe-based alloy series exhibited a sufficient PBF-LB process robustness (Supplementary Fig. 1b and Fig. 7a). Microstructural investigations of Al-Fe-X ternary alloys (X: Cu, Mn, and Ti) confirm the distinct roles of these alloying elements in influencing microstructure and mechanical properties: Cu and Mn act as eutectic-type stabilizers of the Al_6Fe phase, while Ti functions as a peritectic-type element with high solubility. Additionally, the addition of Ti promotes grain refinement through the heterogeneous nucleation of nanosized Al_3Ti-phase particles during solidification, thereby enhancing the tensile ductility of the material. The combined addition of alloying elements that stabilize the Al_6Fe phase further enhances mechanical performance. Furthermore, alloying elements with distinct roles can be independently partitioned during solidification, enabling precise control over the elemental distribution in the α-Al/Al_6Fe two-phase microstructures formed via the PBF-LB process. Stabilizing the Al_6Fe phase (in terms of thermodynamics) might contribute to a slight variation in the α-Al/Al_6Fe two-phase microstructure depending on local thermal histories in the PBF-LB process, suggesting high processing reproducibility and low process-window sensitivity for the Al-Fe-based alloy series. Further research should explore design strategies for optimizing these alloys for various functional applications. This study highlights the potential of incorporating refined metastable phases, formed during rapid solidification, into the design of high-performance Al alloys for laser AM technologies (including the PBF-LB process). Based on the

aforementioned results and discussion, the proposed design concept would be applicable to other alloy systems (e.g., steel, Ti alloys, and Ni-based alloys) in terms of elemental partitioning between liquid and solid phases (Fig. 1e).

Methods

Manufacturing process

Experimental powders comprising different compositions of Al-Fe-based ternary and quaternary alloys with average particle sizes below 20 µm were gas-atomized by Toyo Aluminum K.K. The morphologies of these alloy powders are presented in Supplementary Fig. 13. The observed particle morphologies appeared somewhat irregular, whereas these powders exhibited sufficient flowability for bedding on the base plate in the present study. The chemical compositions of the initial alloy powders and PBF-LB-processed samples were determined using inductively coupled plasma-atomic emission spectrometry (ICP-AES), and the results are summarized in Supplementary Table 4. Additive manufacturing was performed using a PBF-LB instrument (ProX DMP 200, 3D Systems, Rock Hill, SC, USA) under an Ar atmosphere, with oxygen levels maintained below 500 ppm. The manufacturing process utilized a Yb laser (wavelength: 1070 nm) with a laser power (P) of 102–204 W, scan speed (v) of 0.6–1.4 m/s, hatch spacing of 100 µm, powder layer thickness of 30 µm, and laser spot size of approximately 100 µm in diameter. Twenty-five rectangular samples ($15 \times 15 \times 10$ mm^3) were fabricated under varying P and v conditions (Supplementary Fig. 1a). The densities of the fabricated samples were measured at ambient temperature using Archimedes' method. The relationship between relative density and deposited energy density[33] ($P{\cdot}v^{-1/2}$) was analyzed to determine the optimal laser conditions for alloy densification (Supplementary Figs. 1b and 7a). The optimized laser parameters are provided in Supplementary Table 1. These parameters were then applied to fabricate larger rectangular samples (Supplementary Fig. 7b) for tensile test specimens (4 mm in diameter, 20 mm gauge length) with the TD either parallel or perpendicular to the BD. To evaluate the thermal stability of mechanical properties, the Al-Fe-Mn-Ti quaternary alloy sample was exposed to an elevated temperature of 300 °C for various periods, ranging from 1 to 300 h. Uniaxial tensile tests were conducted at temperatures ranging from ambient temperature (20 °C) to 300 °C at a constant strain rate of 1.0×10^{-3} s^{-1}. Three measurements were performed on alloy samples at each temperature. The fracture surfaces were examined using SEM (JEOL JSM-IT510).

Microstructural characterizations

Microstructures were analyzed using optical microscopy, XRD, SEM, EBSD, and TEM. The samples for optical microscopy were mechanically polished and etched using a hydrofluoric acid solution (5 vol%). XRD was performed using a Rigaku Ultima IV instrument with a Cu target voltage of 40 V and current of 40 mA. SEM was performed using a field-emission SEM instrument (JEOL JSM-7001F) equipped with an EBSD detector operated at 30 kV. The conventional EDAX digital detector was used to capture the EBSD pattern. The applied step size and quality metrics parameters of the EBSD data measured in this study are listed in Supplementary Table 5. The artifacts at the grain boundaries (typically 1 pixel) for preparing orientation distribution maps were cleaned using a cleanup process in OIM analysis software (Version 6.1). Quantitative analyses of the refined Al_6Fe phase were performed using a low-voltage SEM (in-lens type microscope, Carl Zeiss ULTRA 55) at a voltage of 1.0 kV for high-resolution observations. We relied on bright-field and high-angle annular dark-field (HAADF) imaging using a field-emission type TEM (JEOL JEM-2100F/HK) operated at 200 kV. TEM bright-field images were captured using an image software of DigitalMicrograph Version 2.30 (Gatan, Inc.) We performed STEM energy-dispersive X-ray spectroscopy (EDS) for elemental mapping and quantitative chemical composition analysis using the NSS4 X-ray Microanalysis Version 3.3 analysis software (Thermo Fisher Scientific Inc.). TEM thin samples were prepared using the ion milling system (JEOL EM-09100IS).

Data availability

EBSD data and mechanical property data for each alloy specimen are deposited in the Figshare system (https://doi.org/10.6084/m9.figshare.28463321). Data supporting the findings of this study are available in this article, the supplementary material, and all source data provided within the Source Data file. Data is available from the corresponding author on request.

References

1. Sames, W. J., List, F. A., Pannala, S., Dehoff, R. R. & Babu, S. S. The metallurgy and processing science of metal additive manufacturing. *Inter. Mater. Rev.* **61**, 315–360 (2016).
2. DebRoy, T. et al. Additive manufacturing of metallic components – process, structure and properties. *Prog. Mater. Sci.* **92**, 112–224 (2018).
3. Yadroitsev, I., Yadroitsava, I., & Du Plessis, A. Basics of laser powder bed fusion. In *Fundamentals of Laser Powder Bed Fusion of Metals* 15–38 (Elsevier, Amsterdam, 2021).
4. Blakey-Milner, B. et al. Metal additive manufacturing in aerospace: a review. *Mater. Des.* **209**, 110008 (2021).
5. Careri, F., Khan, R. H. U., Todd, C. & Attallah, M. M. Additive manufacturing of heat exchangers in aerospace applications: a review. *Appl. Therm. Eng.* **235**, 121387 (2023).
6. Smith, T. M. et al. A 3D printable alloy designed for extreme environments. *Nature* **617**, 513–518 (2023).
7. Takata, N., Kodaira, H., Sekizawa, K., Suzuki, A. & Kobashi, M. Change in microstructure of selectively laser melted AlSi10Mg alloy with heat treatments. *Mater. Sci. Eng. A* **704**, 218–228 (2017).
8. Kotadia, H. R., Gibbons, G., Das, A. & Howes, P. D. A review of laser powder bed fusion additive manufacturing of aluminium alloys: microstructure and properties. *Addit. Manuf.* **46**, 102155 (2021).
9. Fiocchi, J., Tuissi, A. & Biffi, C. A. Heat treatment of aluminium alloys produced by laser powder bed fusion: a review. *Mater. Des.* **204**, 109651 (2021).
10. Zhao, L. et al. Review on the correlation between microstructure and mechanical performance for laser powder bed fusion AlSi10Mg. *Addit. Manuf.* **56**, 102914 (2022).
11. Takata, N., Liu, M., Li, H., Suzuki, A. & Kobashi, M. Fast scanning calorimetry study of Al alloy powder for understanding microstructural development in laser powder bed fusion. *Mater. Des.* **219**, 110830 (2022).
12. Yun, M. & Jung, I.-H. Development of a rapid solidification model for additive manufacturing process and application to Al-Si alloy. *Acta Mater.* **265**, 119638 (2024).
13. Takata, N., Liu, M., Kodaira, H., Suzuki, A. & Kobashi, M. Anomalous strengthening by supersaturated solid solutions of selectively laser melted Al–Si-based alloys. *Addit. Manuf.* **33**, 101152 (2020).
14. Dan, C. et al. Achieving ultrahigh fatigue resistance in AlSi10Mg alloy by additive manufacturing. *Nat. Mater.* **22**, 1182–1188 (2023).
15. Gong, S. et al. Wear properties of aluminum alloys fabricated by laser powder bed fusion. *Tribol. Int.* **187**, 108769 (2023).
16. Linder, C. et al. Corrosion resistance of additively manufactured aluminium alloys for marine applications. *npj Mater. Degrad.* **8**, 46 (2024).
17. Hoshi, Y. et al. Four-dimensional electrochemical impedance spectroscopy: role of microstructure on corrosion behaviour of Al-Si alloys additive-manufactured by laser powder bed fusion. *Corros. Sci.* **232**, 112018 (2024).
18. Takata, N., Liu, M., Suzuki, A., Kobashi, M. & Kato, M. Negative strain rate sensitivity of yield strength of Al-Si alloy additive-manufactured using laser powder bed fusion. *Scr. Mater.* **213**, 114635 (2022).

19. Guercio, G. D. et al. Cracking behaviour of high-strength AA2024 aluminium alloy produced by laser powder bed fusion. *Addit. Manuf.* **54**, 102776 (2022).
20. Malek, G. E. N. C. et al. Optimization of the strength vs. conductivity trade-off in an aluminium alloy designed for laser powder bed fusion. *Mater. Sci. Eng. A* **858**, 144139 (2022).
21. Martin, J. H. et al. 3D printing of high-strength aluminium alloys. *Nature* **549**, 365–369 (2017).
22. Luo, Y. et al. Effects of microstructure heterogeneity and defects on mechanical behavior of Zr modified AA7075 manufactured by laser powder bed fusion. *Addit. Manuf.* **97**, 104626 (2025).
23. Kou, S. A criterion for cracking during solidification. *Acta Mater.* **88**, 366–374 (2015).
24. Chen, Y. et al. In situ observation and reduction of hot-cracks in laser additive manufacturing. *Commun. Mater.* **5**, 84 (2024).
25. Mishra, R. S. & Thapliyal, S. Design approaches for printability-performance synergy in Al alloys for laser-powder bed additive manufacturing. *Mater. Des.* **204**, 109640 (2021).
26. Dreano, A. et al. Computational design of a crack-free aluminum alloy for additive manufacturing. *Addit. Manuf.* **55**, 102876 (2022).
27. Liu, G. & Müller, D. B. Addressing sustainability in the aluminum industry: a critical review of life cycle assessments. *J. Clean. Prod.* **35**, 108–117 (2012).
28. Raabe, D. et al. Making sustainable aluminum by recycling scrap: the science of "dirty" alloys. *Prog. Mater. Sci.* **128**, 100947 (2022).
29. Allen, C. M., O'Reilly, K. A. Q., Cantor, B. & Evans, P. V. Intermetallic phase selection in 1XXX Al alloys. *Prog. Mater. Sci.* **43**, 89–170 (1998).
30. Qi, X., Takata, N., Suzuki, A., Kobashi, M. & Kato, M. Managing both high strength and thermal conductivity of a laser powder bed fused Al–2.5 Fe binary alloy: effect of annealing on microstructure. *Mater. Sci. Eng. A* **805**, 140591 (2021).
31. Kimura, T., Nakamoto, T., Ozaki, T. & Miki, T. Microstructures and mechanical properties of aluminum-transition metal binary alloys (Al-Fe, Al-Mn, and Al-Cr) processed by laser powder bed fusion. *J. Alloy. Compd.* **872**, 159680 (2021).
32. Wu, Y. et al. Microstructure and mechanical property evolution of additive manufactured eutectic Al-2Fe alloy during solidification and aging. *J. Alloy. Compd.* **897**, 163243 (2022).
33. Qi, X., Takata, N., Suzuki, A., Kobashi, M. & Kato Laser powder bed fusion of a near-eutectic Al–Fe binary alloy: processing and microstructure. *Addit. Manuf.* **35**, 101308 (2020).
34. Michi, R. A., Plotkowski, A., Shyam, A., Dehoff, R. R. & Babu, S. S. Towards high-temperature applications of aluminium alloys enabled by additive manufacturing. *Int. Mater. Rev.* **67**, 298–345 (2022).
35. de Araujo, A. P. M. et al. Additive manufacturing of a quasicrystal-forming Al95Fe2Cr2Ti1 alloy with remarkable high-temperature strength and ductility. *Addit. Manuf.* **41**, 101960 (2021).
36. Kimura, T. et al. Microstructural development and aging behavior of Al–Cr–Zr heat-resistant alloy fabricated using laser powder bed fusion. *J. Mater. Res. Technol.* **15**, 4193–4207 (2021).
37. Michi, R. A. et al. A creep-resistant additively manufactured Al-Ce-Ni-Mn alloy. *Acta Mater.* **227**, 117699 (2022).
38. Pérez-Prado, M. T., Martin, A., Shi, D. F., Milenkovic, S. & Cepeda-Jiménez, C. M. An Al-5Fe-6Cr alloy with outstanding high temperature mechanical behavior by laser powder bed fusion. *Addit. Manuf.* **55**, 102828 (2022).
39. Kimura, T. et al. Combined factors for enhanced high-temperature strength of Al-Mn-Cr heat-resistant alloy fabricated using laser-based powder bed fusion. *Mater. Char.* **196**, 112618 (2023).
40. Luo, G. et al. Improved elevated-temperature strength and thermal stability of additive manufactured Al–Ni–Sc–Zr alloys reinforced by cellular structures. *Addit. Manuf.* **90**, 104313 (2024).
41. Shang, A. et al. Additive manufacturing of an ultrastrong, deformable Al alloy with nanoscale intermetallics. *Nat. Commun.* **15**, 5122 (2024).
42. Wu, C., Wen, J., Zhang, J., Song, B. & Shi, Y. Additive manufacturing of heat-resistant aluminum alloys: a review. *Int. J. Extrem. Manuf.* **6**, 062013 (2024).
43. Shi, Q. et al. Additively manufactured fine-grained Al–Fe–Cu-Sc-Zr alloy with resistance to brittleness under high temperature. *J. Mater. Res. Technol.* **33**, 7310–7324 (2024).
44. Pauzon, C. et al. Direct ageing of LPBF Al-1Fe-1Zr for high conductivity and mechanical performance. *Acta Mater.* **258**, 119199 (2023).
45. Cheng, Y. et al. Laser-beam powder bed fusion of Al–Fe–Cu alloy to achieve high strength and thermal conductivity. *Addit. Manuf. Lett.* **8**, 100191 (2024).
46. Okano, N., Takata, N., Suzuki, A. & Kobashi, M. Effects of Mn and Cu additions on solidification microstructure and high-temperature strength of cast Al–Fe binary alloy. *Mater. Trans.* **64**, 492–499 (2023).
47. Nicol, A. D. I. The structure of $MnAl_6$. *Acta Cryst.* **6**, 285–293 (1953).
48. Black, P. J., Edwards, O. S. & Forsyth, J. B. The structure of alpha (Al-Cu-Fe). *Acta Cryst.* **14**, 993–998 (1961).
49. Walnsch, A., Kriegel, M. J., Fabrichnaya, O. & Leineweber, A. Thermodynamic assessment and experimental investigation of the systems Al–Fe–Mn and Al–Fe–Mn–Ni. *Calphad* **66**, 101621 (2019).
50. Raghavan, V. Al-Cu-Fe (Aluminum-Copper-Iron). *J. Phase Equilib. Diffus.* **31**, 449–452 (2010).
51. Walford, L. K. The structure of the intermetallic phase $FeAl_6$. *Acta Cryst.* **18**, 287–291 (1965).
52. Ghosh, S. et al. Modeling of hierarchical solidification microstructures in metal additive manufacturing: challenges and opportunities. *Addit. Manuf.* **78**, 103845 (2023).
53. Aziz, M. J. Model for solute redistribution during rapid solidification. *J. Appl. Phys.* **53**, 1158–1168 (1982).
54. Du, Y. et al. Diffusion coefficients of some solutes in fcc and liquid Al: critical evaluation and correlation. *Mater. Sci. Eng. A* **363**, 140–151 (2003).
55. Wang, W., Takata, N., Suzuki, A., Kobashi, M. & Kato, M. Design of Al–Fe–Mn alloy for both high-temperature strength and sufficient processability of laser powder bed fusion. *Addit. Manuf.* **68**, 103524 (2023).
56. Roscher, M., Balachandran, S., Mayweg, D. & Jägle, E. Development of Al-Ti-based alloys for laser powder bed fusion. *Addit. Manuf.* **47**, 102315 (2021).
57. Yan, K. et al. Nucleation and growth of Al_3Sc precipitates during isothermal aging of Al-0.55 wt% Sc alloy. *Mater. Char.* **179**, 111331 (2021).
58. Otani, Y., Takata, N., Suzuki, A., Kobashi, M. & Kato, M. Effect of heat treatments on inhomogeneous deformation of the melt-pool structure of Al–Si alloy manufactured via laser powder bed fusion. *Mater. Sci. Eng. A* **909**, 146808 (2024).
59. Knipling, K. E., Dunand, D. C. & Seidman, D. N. Criteria for developing castable, creep-resistant aluminum-based alloys: a review. *Int. J. Mater. Res.* **97**, 246–265 (2006).
60. Li, R., Kondo, M., Suzuki, T., Suzuki, A. & Takata, N. Controlling the addition of solute Ti in Al-Mg-Zn-Cu-Ni alloy for enhanced high-temperature creep properties. *Mater. Sci. Eng. A* **889**, 145859 (2024).

Acknowledgements

We gratefully acknowledge financial support from "JST PRESTO (Japan): Grant Number JP22688912" and "JSPS KAKENHI (Japan): Grant Number: 24H00378". Experimental material processing was supported by "Knowledge Hub Aichi (Japan)" and the "Priority Research Project of the Aichi Prefectural Government (Japan)." We are thankful for the generous

assistance and guidance of Mr. Kimitaka Higuchi of the Institute of Materials and Systems for Sustainability, Nagoya University (Japan), in TEM operations.

Author contributions

N.T., K.M., T.M., and M.K. (Masaki Kato) fabricated all the alloy samples and optimized the processing parameters. K.M., T.M., Y.C., Y.X., and W.W. performed microstructural characterization (OM, SEM, XRD, and EBSD) and mechanical testing. N.T., W.W., and D.K. performed the TEM characterization and analyses. N.T. conducted the thermodynamic calculations. D.K., A.S., and M.K. (Makoto Kobashi) validated the results. N.T. drafted the initial manuscript, and D.K., A.S., and M.K. (Makoto Kobashi) edited it. N.T. conceived, designed, and led the study. All co-authors contributed to the data analysis and discussion.

Competing interests

The authors declare no competing interests.

Additional information

Supplementary information The online version contains supplementary material available at https://doi.org/10.1038/s41467-025-67281-8.

Correspondence and requests for materials should be addressed to Naoki Takata.

Peer review information *Nature Communications* thanks Lv Zhao, Mathiyazhagan Sathishkumar, and Takashi Maeshima for their contribution to the peer review of this work. A peer review file is available.